

Microburst Size Distribution Derived with AeroCube-6

M. Shumko¹, A. Johnson¹, J. Sample¹, B.A. Griffith¹, D.L. Turner², T.P. O'Brien², O. Agapitov³, J.B. Blake², S. G. Claudepierre²

¹Department of Physics, Montana State University, Bozeman, Montana, USA

²Space Science Applications Laboratory, The Aerospace Corporation, El Segundo, California, USA

³Space Sciences Laboratory, University of California Berkeley, Berkeley, California, USA

Key Points:

- The dual AeroCube-6 CubeSats simultaneously observed > 35 keV microbursts at a variety of spatial separations ranging from 2 to ≈ 100 km.
- In low Earth orbit the majority of microbursts have a size on the order of a few tens of km.
- At the magnetic equator, the size of most microbursts corresponds to the size of whistler-mode chorus wave packets.

Corresponding author: M. Shumko, msshumko@gmail.com

Abstract

Microbursts are an impulsive increase of electrons from the radiation belts into the atmosphere and have been directly observed in low Earth orbit and the upper atmosphere. Prior work has estimated that microbursts are capable of rapidly depleting the radiation belt electrons on the order of a day, hence their role to radiation belt electron losses must be considered. Losses due to microbursts are not well constrained, and more work is necessary to accurately quantify their contribution as a loss process. To address this question we present a statistical study of > 35 keV microburst sizes using the pair of AeroCube-6 CubeSats. The microburst size distribution in low Earth orbit and the magnetic equator was derived using both spacecraft. In low Earth orbit, the majority of microbursts were observed while the AeroCube-6 separation was less than a few tens of km, mostly in latitude. To account for the statistical effects of random microburst locations and sizes, a Monte Carlo and analytic models were developed to test hypothesized microburst size distributions. A family of microburst size distributions were tested and a Markov Chain Monte Carlo sampler was used to estimate the optimal distribution of the microburst size model parameters. Finally, a majority of observed microbursts map to sizes less than 200 km at the magnetic equator. Since microbursts are widely believed to be generated by scattering of radiation belt electrons by whistler mode waves, the observed microburst size correlates to coherent whistler mode chorus sizes derived in prior literature.

1 Plain Language Summary

Electron microbursts are a sub-second, impulsive form of electron precipitation from the radiation environment right above Earth's atmosphere. They are believed to cause complete loss of electrons on the order of a day from the near-Earth radiation belt environment. To make these estimates, researchers need to make simplifying assumptions. These assumptions reduce the accuracy of loss estimates by an unknown amount and it is necessary to understand these assumptions. This paper focuses on one assumption needed to calculate how many electrons are lost per microburst, the physical size of microbursts. This study is achieved by using a pair of AeroCube-6 CubeSats that are orbiting a few hundred kilometers above Earth's surface. We find that most microbursts have a size less than a few tens of kilometers and some are as large as one hundred kilometers at AeroCube-6's altitude. Furthermore, we found that the small microbursts correspond to a very small region where microbursts are believed to be generated in the heart of the radiation belts.

2 Introduction

Since the discovery of the Van Allen radiation belts in the 1960s by Van Allen (1959) and Vernov and Chudakov (1960), decades of research has made headway in understanding the various particle acceleration and loss mechanisms. One of the extensively studied mechanisms responsible for both acceleration and loss is wave-particle scattering between whistler-mode chorus waves and electrons (Abel & Thorne, 1998; Meredith et al., 2002; Horne & Thorne, 2003; Thorne et al., 2005; Millan & Thorne, 2007; Bortnik et al., 2008). Whistler-mode chorus waves are typically generated by a temperature anisotropy of low energy electrons up to tens of kiloelectronvolts (keV) and are typically found in the $\sim 0 - 12$ magnetic local times (MLT) (Li, Thorne, Angelopoulos, Bortnik, et al., 2009; Li, Thorne, Angelopoulos, Bonnell, et al., 2009). Whistler-mode chorus waves interact with radiation belt electrons, and are widely believed to cause electron precipitation termed microbursts (e.g., Millan & Thorne, 2007).

Microbursts are a subsecond impulse of electrons that are observed by high altitude balloons and satellites in low Earth orbit (LEO) on radiation belt magnetic footprints $\sim 4-8$ L-shell (L) (e.g., Anderson & Milton, 1964; Lorentzen, Blake, et al., 2001;

O'Brien et al., 2003; Tsurutani et al., 2013; Woodger et al., 2015; Crew et al., 2016; Breneman et al., 2017; Mozer et al., 2018; Greeley et al., 2019), mostly in the dawn MLTs, and with an enhanced occurrence rate during disturbed magnetospheric times (O'Brien et al., 2003; Douma et al., 2017). Microburst's role as a radiation belt electron loss mechanism has been estimated to be significant, with total radiation belt electron depletion due to microbursts estimated to be on the order of a day or less (Lorentzen, Looper, & Blake, 2001; O'Brien et al., 2004; Thorne et al., 2005; Breneman et al., 2017; ?, ?). These average microburst loss estimates are not well constrained due to assumptions made regarding the microburst precipitation region.

One of the unconstrained microburst parameters that is critical to better quantify the role of microbursts as an instantaneous loss mechanism (the number of electrons lost per microburst) is their physical size. Historically, after the bremsstrahlung X-ray signatures of microbursts were discovered by Anderson and Milton (1964), numerous microburst size studies were done using other balloon flights in the mid 1960s. Brown et al. (1965) used data from a pair of balloons separated by 150 km, mainly in longitude, and found that one third of all microbursts observed were temporally coincident. Trefall et al. (1966) then used the results from Brown et al. (1965) to model the probability that a microburst will be observed by two balloons as a function of the radius of the microburst, radius of the precipitating area a balloon is sensitive to, and the balloon separation. Trefall et al. (1966) concluded that the microbursts reported by Brown et al. (1965) must have had a diameter of 230 km assuming a balloon has a circular field of view with a 140 km diameter (for electrons stopped at 100 km altitudes). Soon after, Barcus et al. (1966) used a pair of balloons and concluded that a microburst must have a < 200 km longitudinal extent. Then Parks (1967) used data from a single balloon with four collimated scintillators oriented in different directions and found that the size of some mostly low energy microbursts to have a diameter of 80 ± 28 km, and others were less than 40 km.

Direct observations of microburst electrons are made by LEO spacecraft. J. Blake et al. (1996) found a microburst with a size of a few tens of km using the the Solar Anomalous and Magnetospheric Particle Explorer (SAMPEX) and concluded that typically microbursts are less than a few tens of electron gyroradii in size (order of a few km in LEO). Recently, Dietrich et al. (2010) used SAMPEX observations in another case study and concluded that the observed microbursts were smaller than 4 km. Crew et al. (2016) used the Focused Investigation of Relativistic Electron Bursts: Intensity, Range, and Dynamics (FIREBIRD-II) CubeSats and found an example of a microburst larger than 11 km. Lastly, Shumko et al. (2018) also used FIREBIRD-II to identify a microburst with a size greater than 51 ± 1 km. If anything, the large variance in prior results imply that there is a distribution of microburst scale sizes which this study aims to estimate.

Besides addressing the instantaneous radiation belt electron losses due to individual microbursts, the microburst size distribution is useful to identify the wave mode(s) responsible for scattering microbursts. By mapping the microburst size distribution in LEO to the magnetic equator it can be compared to the wave sizes estimated in prior literature. This comparison can be used to identify the waves and their properties (e.g. amplitude or coherence) responsible for scattering microburst electrons.

This paper addresses these two questions by expanding the prior microburst size case studies by analyzing microburst observations over a three year time period to estimate the microburst size distribution in LEO and the magnetic equator. The twin AeroCube-6 (AC6) CubeSats are utilized for this study because they were ideally equipped to observe microbursts simultaneously over a span of three years while their total separation varied between 2 and 800 km, mostly in latitude (in-track in orbit). This paper first describes the AC-6 mission, including their orbit and instrumentation in section 3. Section 4.1 develops the methodology used to identify microbursts observed by each spacecraft and how they were combined to make a list of simultaneously observed microbursts. Section 4.2 describes the methodology used to estimate the microburst size distributions

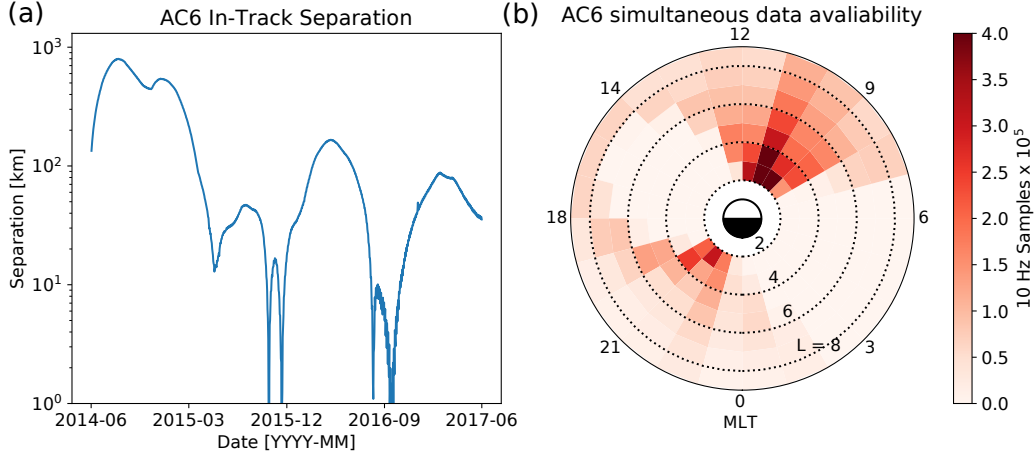


Figure 1. AC6 mission properties for (a) spacecraft separation and (b) number of simultaneous quality 10 Hz samples as a function of L and MLT.

in LEO and the magnetic equator as a function of AC6 separation. Then a model is developed to shed light on how the compounding effects of a hypothesized microburst shape, size distribution, and random microburst locations will be observed by AC6, a two-point measurement platform. Lastly, in section 6 we discuss these results and compare the microburst sizes estimated here to the size distribution of the whistler-mode chorus waves that are believed to cause microbursts.

3 Instrumentation

The AC6 mission consists of a pair of 0.5U (10x10x5 cm) CubeSats built by The Aerospace Corporation and launched on June 19th, 2014 into a 620 x 700 km, 98° inclination orbit. The two satellites, designated as AC6-A and AC6-B, separated after launch and drifted apart. Both AC6 units have an active attitude control system which allows them to adjust the atmospheric drag experienced by each AC6 unit by orienting their solar panel “wings” with respect to the ram direction. By changing their orientation, AC6 was able to achieve fine separation control and maintain a separation between 2-800 km. Figure 1a shows the AC6 separation for the duration of the mission. Figure 1b shows where AC6 was taking 10 Hz data simultaneously as a function of L and MLT which highlights that most data was taken at 8-12 MLT, an ideal local time for observing microbursts. Lastly Fig. 1b shows that the AC6 orbit was roughly dawn-dusk, sun-synchronous and precessed only a few hours in MLT over a three year period.

Each AC6 unit is equipped with three Aerospace microdosimeters (licensed to Teledyne Microelectronics, Inc). The dosimeter used for this study is dos1 and is identical on both AC6 units. Dos1 has a 35 keV electron threshold and all dosimeters sample at 1 Hz in survey mode, and 10 Hz in burst mode in the radiation belts. More detailed technical information on AC6 is described in O’Brien et al. (2016).

4 Methodology

4.1 Microburst Detection

The first step to find microbursts observed simultaneously by AC6 is to identify them on each individual spacecraft. Microbursts were detected with two different meth-

ods that yielded quantitatively similar results. The first method is the burst parameter (O'Brien et al., 2003). This algorithm has been successfully used in other microburst studies, mainly with the microbursts observed by SAMPEX (e.g. O'Brien et al., 2003; Blum et al., 2015; Douma et al., 2017). For AC6, a burst parameter threshold of 5 was determined to be a good trade-off between false positive and false negative microburst detections. Another microburst detection algorithm based on wavelet spectra frequency filtering was developed and the resulting list of microbursts is similar to the list from the burst parameter.

With the two microburst detection lists in hand, data cleaning to remove microburst-like transmitter noise was necessary. The transmitters on AC6 can cause unphysical count impulses in the dosimeters that resembles periodic trains of microbursts. One source of transmitter noise was observed at times when AC6 was in contact with the ground stations above the US for data downloads and commanding, thus the microburst detections made above the US that were mostly at low L were discarded.

Another source of noise is crosslink transmissions between AC6-A and AC6-B. These transmissions occurred when either spacecraft transitioned from the survey mode to 10 Hz mode. This noise is sometimes not caught by the data quality flag, so the following empirically-derived criteria were developed to remove those detections. The dosimeter with a 250 keV nominal electron threshold, dos2, was used because it had a nearly identical response to noise while rarely responded to microbursts. Since the transmitter noise is very periodic with a ≈ 0.2 s period, cross-correlation (CC) and autocorrelation (AC) methods were applied to the dos1 and dos2 time series. Detections were discarded if the following two criteria were met: either dos1 or dos2 time series had a AC peak at a 0.2 or 0.4 s lag and the dos1-dos2 CC was greater than 0.9. The AC lag criteria alone sometimes falsely removed legitimate trains of microbursts, so the second criteria insured that the detection was removed if there was also an unphysically high correlation across an order of magnitude in energy.

The lists of microbursts observed individually by AC6 were then merged into a list of temporally correlated microbursts, i.e. microbursts that were observed simultaneously by both AC6 units, with the following procedure. The general idea is that a microburst detected by one spacecraft will cross-correlate well with the time series from the other spacecraft if it observed a similar microburst, and poorly if there was no microburst observed by the other spacecraft. Each microburst detection made by either spacecraft was cross-correlated with the time series from the other spacecraft whether or not a microburst was observed by the other spacecraft. Cross-correlation windows with 1 and 1.2 s widths were chosen with slightly different window sizes to account for random count variation due to Poisson noise. Microbursts detections that had a cross-correlation greater than 0.8 were considered temporally coincident. This CC threshold was chosen as it is low enough to accept user-identified temporally coincident microbursts superposed with noise, and high enough to reject most non-coincident events. Figure 2, panels (a), (c), (e), and (g) show examples of microbursts observed by both AC6 units when they were separated by 5, 16, 37, and 69 km, respectively.

The last criteria requires that the temporal CC must be greater than the spatial CC + 0.3. The spatial CC was calculated by shifting one spacecraft's time series by the in-track lag to cross-correlate in the same spatial location, i.e. latitude. This criteria was applied to remove curtains, stationary structures observed by AC6 that are narrow in latitude (J. B. Blake & O'Brien, 2016) that can be misidentified as microbursts. Figure 2, panels (b), (d), (f), and (h) show the shifted time series to confirm that there were no spatially correlated, non-microburst structures present. Lastly the merged microburst list was spot checked by two authors to remove poorly correlated and any duplicate events. After filtering out transmitter noise and applying the CC criteria, 662 simultaneous microburst detections were found and used in this study.

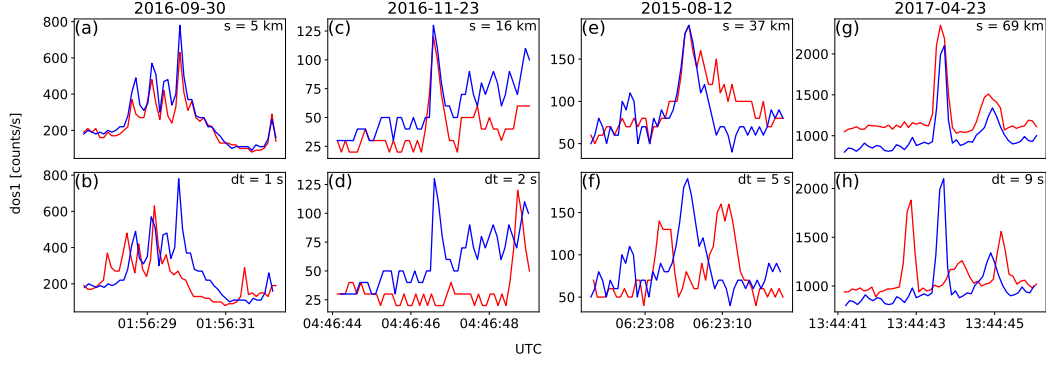


Figure 2. Examples of > 35 keV microbursts observed simultaneously by AC6-A in red and AC6-B in blue. Panels (a), (c), (e), and (g) show the temporally-aligned time series when AC6 were separated by $s = 5, 16, 37$, and 69 km, respectively. The corresponding panels (b), (d), (f), and (h) show the spatially-aligned time series which is made by shifting the AC6-A time series in the above panels by the in-track lag (annotated with dt) that show any spatially correlated structures. The clear temporal correlation and lack of spatial correlation demonstrates that these events are microbursts.

4.2 Microburst Size Distribution in LEO and Magnetic Equator

The temporally coincident microbursts, which from now on will be referred to as microbursts, are now used to estimate the fraction of microbursts observed above AC6 separation, s . When AC6 observes a microburst at s , the microburst's size must be greater than s . This fact, along with the arguments presented in Section 4 in Joy et al. (2002) who studied the most probable Jovian magnetopause and bow shock stand off distances, are used to investigate the dependence of the number of microbursts observed above s , as a function of s . This dependence is the microburst complementary cumulative distribution function $\bar{F}(s)$.

The cumulative fraction of microbursts observed above s is the ratio of $N(s)$, the normalized number of microbursts observed above s , to $N(0)$, the total number of microbursts observed

$$\bar{F}(s) = \frac{N(s)}{N(0)} \quad (1)$$

where $N(s)$ is defined by

$$N(s) = \sum_{i=s}^{\infty} n_i \left(\frac{S_{max}}{S_i} \right) \quad (2)$$

where n_i is the number of microbursts observed by AC6 in i th separation bin. The normalization term S_{max}/S_i is a ratio of the number of 10 Hz samples in the most sampled separation bin to the number of samples in the i th bin. This normalization factor corrects AC6's non-uniform sampling in separation, thus $\bar{F}(s)$ can be interpreted as the fraction of microbursts observed above s assuming AC6 sampled evenly in separation. Microburst $\bar{F}(s)$ in LEO is shown by the black curve in Fig. 3a for $4 < L < 8$ and split into one L -wide bins with the colored curves. The separation bin width used in Fig. 3 is 5 km. To check for bias in $\bar{F}(s)$ due to the choice of separation bins, $\bar{F}(s)$ was resampled using other bin widths and offsets. Bin widths as large as 20–30 km and bin offsets did not qualitatively effect the curves in Fig. 3a. The normalization i.e., the number of 10 Hz samples in each separation bin, is shown in 3c.

The overall trend in Fig. 3a shows a sudden cumulative probability drop off, followed by a shoulder up to $s \approx 70$ km where $\bar{F}(s)$ drops to nearly zero. A large negative gradient of $\bar{F}(s)$ at some separation implies that microbursts must be smaller than that separation. To quantify this, Fig. 3b shows the microburst probability density function (PDF), calculated by differentiating $\bar{F}(s)$. The microburst PDF shows a peak at $s < 30$ km as well as a peak between 70–80 km separation. These PDF peaks are evidence of a sub 30 km microburst population and larger microbursts observed up 70–80 km separations. The shaded region around the black curves in Fig. 3a-b shows the standard error due to counting statistics. The uncertainty due to false coincidence events i.e. two unrelated microbursts lining up in time by random chance was also considered. The microburst duty cycle in a one minute window ($\approx 1 L$) around each microburst was calculated. The false coincidence probability is the square of the duty cycle and was found to be less than 5% for the majority of microbursts. The false coincidence probability for each microburst was then used to randomly remove microbursts and $\bar{F}(s)$ was recalculated in 10^4 trials. The spread in the $\bar{F}(s)$ trial curves with microbursts randomly removed was much smaller than the uncertainty due to counting statistics alone.

To compare the microburst size to the size of their hypothesized progenitor waves, the spacecraft locations during observed microbursts were mapped to the magnetic equator using the Olson-Pfitzer magnetic field model (Olson & Pfitzer, 1982) which is implemented with a Python wrapper for IRBEM-Lib (Boscher et al., 2012). As previously stated, a microburst observed in LEO has a size larger than the spacecraft separation, hence that microburst would also have a size larger than the spacecraft separation after it was mapped to the magnetic equator. Thus the procedure to estimate $\bar{F}(s)$ is identical to the LEO size distribution but with a different normalization. The normalization factors were calculated by mapping every quality AC6 sample to the magnetic equator and binning them by equatorial separation into 100 km wide bins. Figure 4 shows the equatorial microburst size distribution in the same format as Fig. 3. The equatorial PDF trend is similar to LEO and most of the microbursts were observed when the AC6 equatorial separation was less than 200 km.

The results in Figs. 3 and 4 show the fraction of microbursts observed above a spacecraft separation and do not fully represent the microbursts size distribution due to the compounding effects from the range of microburst sizes and random locations of microbursts with respect to AC6 i.e. even if the microburst size is much larger than the AC6 separation, some fraction of those microbursts will be only observed by one AC6 spacecraft. Thus modeling is necessary to capture the compounding influence of these statistical effects on AC6.

5 Modeling the Distribution of Microburst Sizes

5.1 Monte Carlo and Analytic Models to Calculate $\bar{F}(s)$

To account for the effects due to microbursts randomly occurring around AC6 with an unknown distribution of microburst sizes, Monte Carlo (MC) and analytic models were developed. These models assume a hypothesized distribution of microburst sizes expressed with a probability density function $p(d|\theta)$ where θ are the dependent variables, and a microburst footprint shape to estimate $\bar{F}(s)$. The microburst footprint is assumed to be circular with a diameter d . $p(d|\theta)$ can be understood as “the probability of observing a microburst of diameter d , given the parameters θ ”. Various microburst size distributions were considered: a one-size and two-size microburst populations, and continuous $p(d|\theta)$ such as Maxwell, Weibull, and log-normal.

The Monte Carlo model is the most intuitive. It first randomly scatters 10^5 microburst centers in a 400 x 400 km grid around AC6. Then each microburst center was assigned a diameter, randomly picked from a $p(d|\theta)$ distribution after θ parameters were speci-

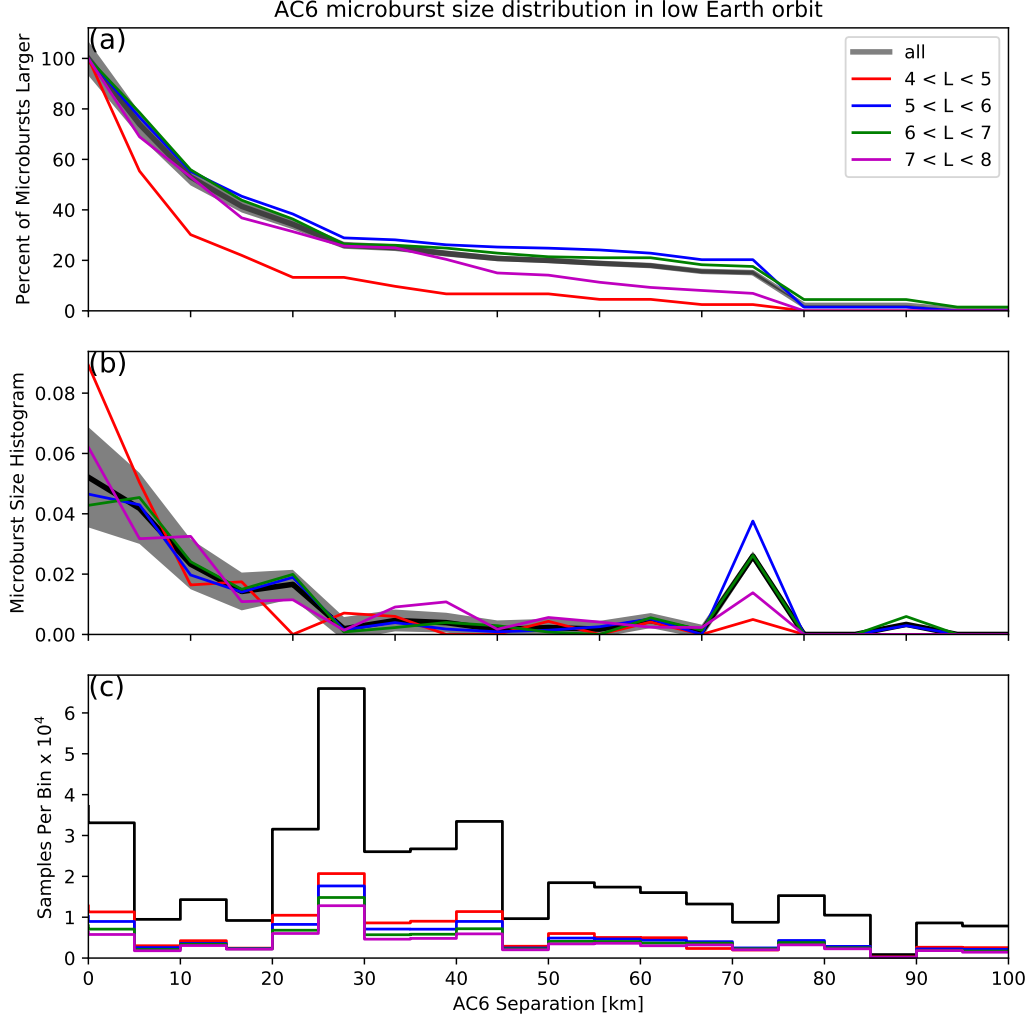


Figure 3. Microburst size distribution in low Earth orbit. Panel (a) shows the percent of microbursts observed above that separation after normalizing for the uneven AC6 sampling in separation. Panel (b) shows the microburst probability density (size histogram) as a function of separation. Lastly, panel (c) shows the normalization, i.e. number of simultaneous samples AC6 observed as a function of separation. The colored lines show the distributions binned by L , and the thick black curve for the entire radiation belt ($4 < L < 8$). The gray shading around the black curve shows the uncertainty due to counting statistics.

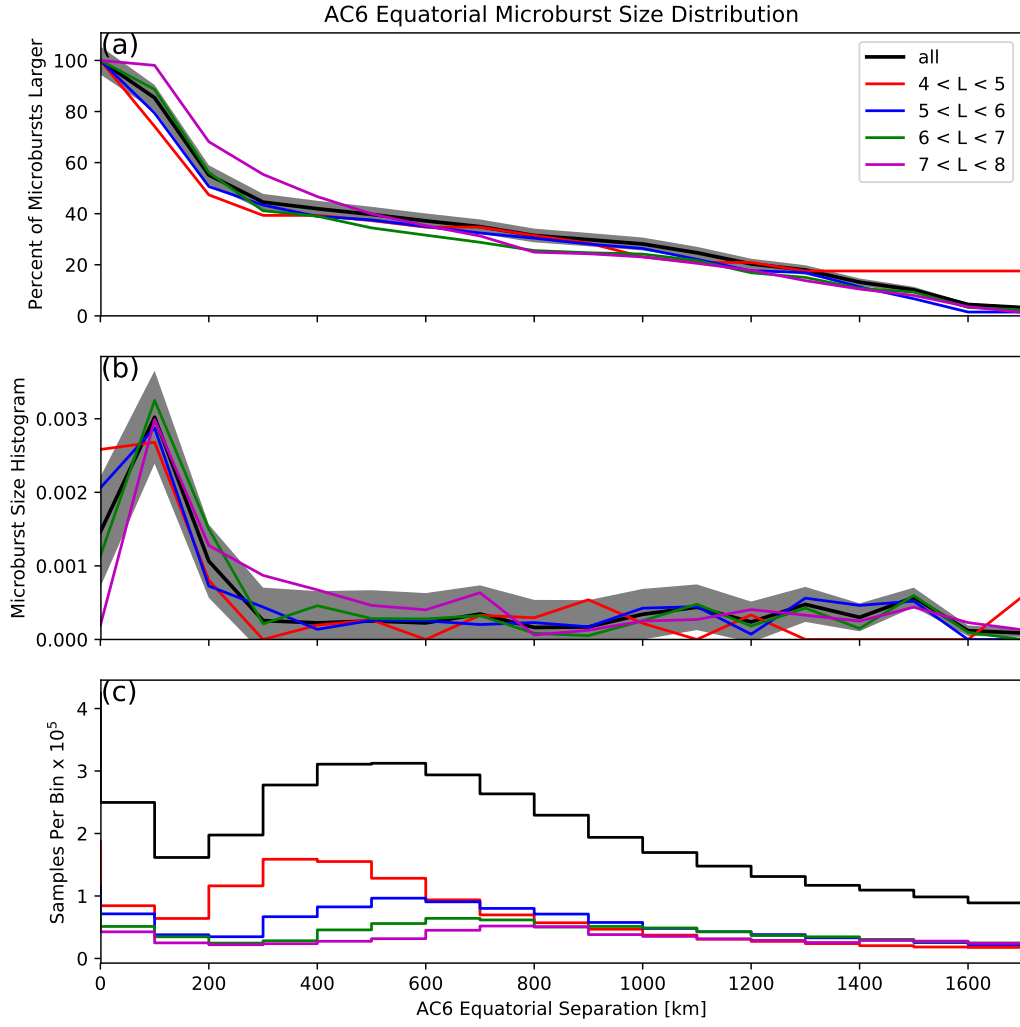


Figure 4. Microburst size distribution mapped to the magnetic equator in the same format as Fig. 3.

Spacecraft A is placed at the origin, and spacecraft B is placed along the positive y-axis at distances from spacecraft A corresponding to the AC6 separation bins used in Section 4.2. Then for each spacecraft B location, the number of microbursts that encompass both spacecraft was counted. The modeled fraction of microbursts observed above s is then

$$\bar{F}(s) = \frac{\sum_{i>s}^{\infty} n_i}{\sum_{i>0}^{\infty} n_i}. \quad (3)$$

where as before the number of microbursts observed by both spacecraft in the i th bin is n_i .

The analytic model, while identical to the MC model, highlights the geometrical concepts connecting $p(d|\theta)$ and $\bar{F}(s)$ with geometry arguments similar to Trefall et al. (1966). For a microburst with $d = 2r \geq s$, there is an area between AC6 where that microburst will be observed by both spacecraft if the microburst's center lands there. Figure 5a-c shows this geometry with the two spacecraft indicated with black dots with varying relations between r and s . All microbursts whose center lies inside the circular area of radius r surrounding either spacecraft will be observed by that spacecraft. If it exists, the intersection of the two circular areas around both spacecraft defines another area, $A(r, s)$ where a microburst will be observed by both spacecraft if the microburst center lands there. This area can be calculated using the circle-circle intersection area equation,

$$A(r, s) = 2r^2 \cos^{-1} \left(\frac{s}{2r} \right) - \frac{s}{2} \sqrt{4r^2 - s^2}. \quad (4)$$

Example geometries where $A(r, s) > 0$ are shown in Fig. 5b and c. With this conceptual model and $A(r, s)$, the analytic form of $\bar{F}(s)$ can be found and is derived in Appendix A. To demonstrate the effects of random microburst locations near AC6, examples of the analytic and Monte Carlo $\bar{F}(s)$ curves are shown in Fig. 5d for a one-size, $d = 40$ km microburst population.

5.2 Methods for estimating optimal θ parameters

At this stage we have all of the ingredients to calculate $\bar{F}(s)$ given a prescribed $p(d|\theta)$. For each $p(d|\theta)$ tested, the optimal θ parameters are estimated in this study using the traditional least squares regression and Bayesian inference. While we report the θ parameters that minimize least squares, this section focuses on Bayesian inference because it seamlessly incorporates statistical uncertainty in the data. The uncertainty in the data is then propagated to θ which is then no longer an optimal value, rather a distribution of values that is consistent with the observations and its uncertainty.

Bayesian inference is rooted in Bayes theorem of conditional probability. Given the observed $\bar{F}(s)$ as y , and model's dependent variables as θ , Bayes theorem can be written as

$$p(\theta|y) = \frac{p(y|\theta)p(\theta)}{p(y)}. \quad (5)$$

$p(\theta)$ is the distribution of θ that describe our prior level of knowledge about that parameter e.g. from earlier microburst size studies, a microburst size must be less than 500 km in LEO. This is called the prior which is quantified by a PDF such as normal, uniform, etc. Next term is the likelihood, $p(y|\theta)$, the conditional probability of obtaining y given a particular θ . The likelihood probability is a probabilistic penalty function that quantifies the discrepancy between the modeled and observed $\bar{F}(s)$ in terms of the standard

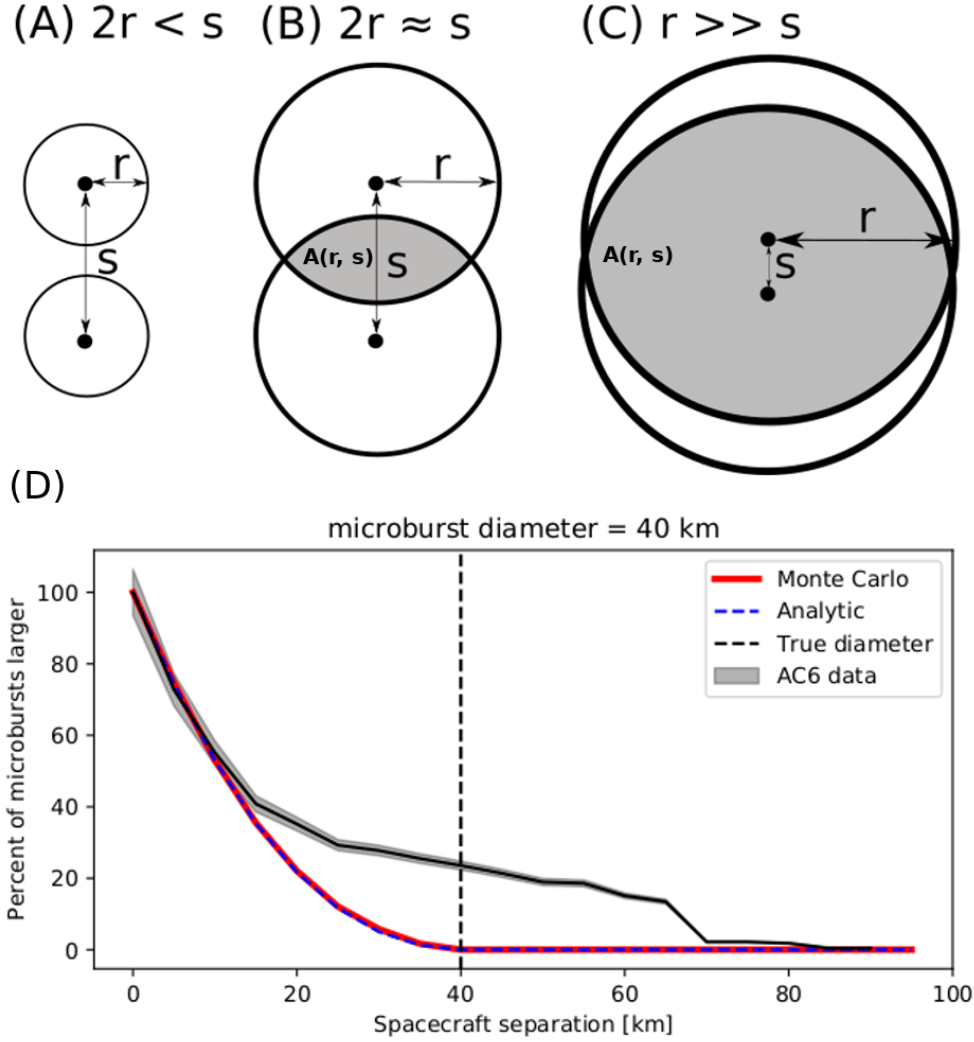


Figure 5. Panels A-C show the varying geometries of the analytic model. The two spacecraft are shown as black dots. The enclosing black circle around each spacecraft bounds the area where a microburst will be observed by one or both AC6 units if the microburst’s center lies inside the circle. Panel (A) shows the case where microburst diameter is smaller than the AC6 separation and all microbursts will be observed by either unit A or B and never simultaneously. Panel (B) shows the intermediate case where the microburst diameter is comparable to the AC6 separation and some fraction of microbursts will be observed simultaneously. The fraction of the microbursts simultaneously observed is proportional to the circle intersection area $A(r, s)$ and is shown with grey shading. Panel (C) shows the case where the microburst diameter is much larger than the spacecraft separation and nearly all microbursts will be observed by both spacecraft. Lastly panel (D) shows $\bar{F}(s)$ from the AC6 data with a solid black line, and modeled MC and analytic $\bar{F}(s)$ curves for a single-sized microburst distribution with $d = 40$ km.

error. The resulting PDF of θ s consistent with the observations is $p(\theta|y)$ known as the posterior distribution. The posterior is an update to our prior distributions, modified by the likelihood i.e. the data and its uncertainties. Here, the posterior is used to make inferences regarding the range of θ parameters that generate a $\bar{F}(s)$ that is consistent with the observations. The last parameter in Bayes theorem is $p(y)$. $p(y)$ is the marginal likelihood (evidence) that describes the probability of obtaining y after marginalizing over all prior variables. Calculation of $p(y)$ is difficult, and often not necessary for model parameter estimation.

With all of the above terminology, the important takeaway is that the posterior distribution for each model parameter is interpreted as the range of our model's dependent parameters that are consistent with the observations. A 95% credible interval (CI) for each model parameter is reported here that is interpreted as: assuming a hypothesized $p(d|\theta)$, there is a 95% probability that the true θ is inside the CI. To sample the posterior distribution, the θ parameter space is explored with a Markov Chain Monte Carlo (MCMC) sampler. In a nutshell a Markov Chain is a process that samples random variables that depend on only the previous state of those random variables. Hence a MCMC sampler is a Monte Carlo sampler that samples the θ parameter space by picking random θ values based on the previous state of θ .

The first and one of the most popular MCMC is the Metropolis-Hastings sampler (Metropolis et al., 1953; Hastings, 1970). While the Metropolis-Hastings sampler is explained in detail in Metropolis et al. (1953) and Hastings (1970) and a good introduction given in Sambridge et al. (2006) as well as Sharma (2017), a brief overview is warranted. The Metropolis-Hastings sampler samples the posterior distribution in N trials. Once an initial set of θ is randomly picked from the prior, the i^{th} trial involves the following steps. First calculate the posterior probability for θ_i . Then pick a proposal θ_{i+1} to jump to, randomly picked near θ_i in parameter space. If the θ_{i+1} posterior probability is higher than θ_i , the MCMC accepts the proposal and moves to θ_{i+1} . If the posterior probability of θ_{i+1} is smaller than θ_i , there is a random chance that θ_{i+1} will be accepted or rejected (if rejected, $\theta_{i+1} = \theta_i$ and a new proposal is generated). This accept/reject criteria allows the sampler to trend to more probable θ while also exploring the neighboring regions. After the N trials, a histogram is made using the accepted θ s to produce the posterior distribution for each model parameter.

5.3 Estimating optimal parameters for various microburst size models

The MCMC sampler is first used to test the simplest microburst size model where all microbursts are one size and the MCMC will estimate that size. The microburst size PDF for this model can be expressed as

$$p(d|d_0) = \delta(d - d_0) \quad (6)$$

where δ is the Dirac Delta function and d_0 is the diameter of all microbursts according to this model. The range of d that are consistent with the observed $\bar{F}(s)$ is shown in Fig. 6. Assuming this model, there is a 95% probability that the microburst diameter is between 38 and 129 km. As a sanity check the optimal size that minimizes least squares is 73 km.

A slight generalization of the one-size model is a two-size microburst population model that assumes the following microburst PDF

$$p(d|d_0, d_1, a) = a\delta(d - d_0) + (1 - a)\delta(d - d_1) \quad (7)$$

where the diameters of the two microburst populations are given by d_0 and d_1 and a is the parameter that quantifies the relative fractions of the two populations. The result of this model is shown in Fig. 7. The fit is slightly better than the one-size model, although that is to be expected given two more free model parameters. A majority, 98 %, of

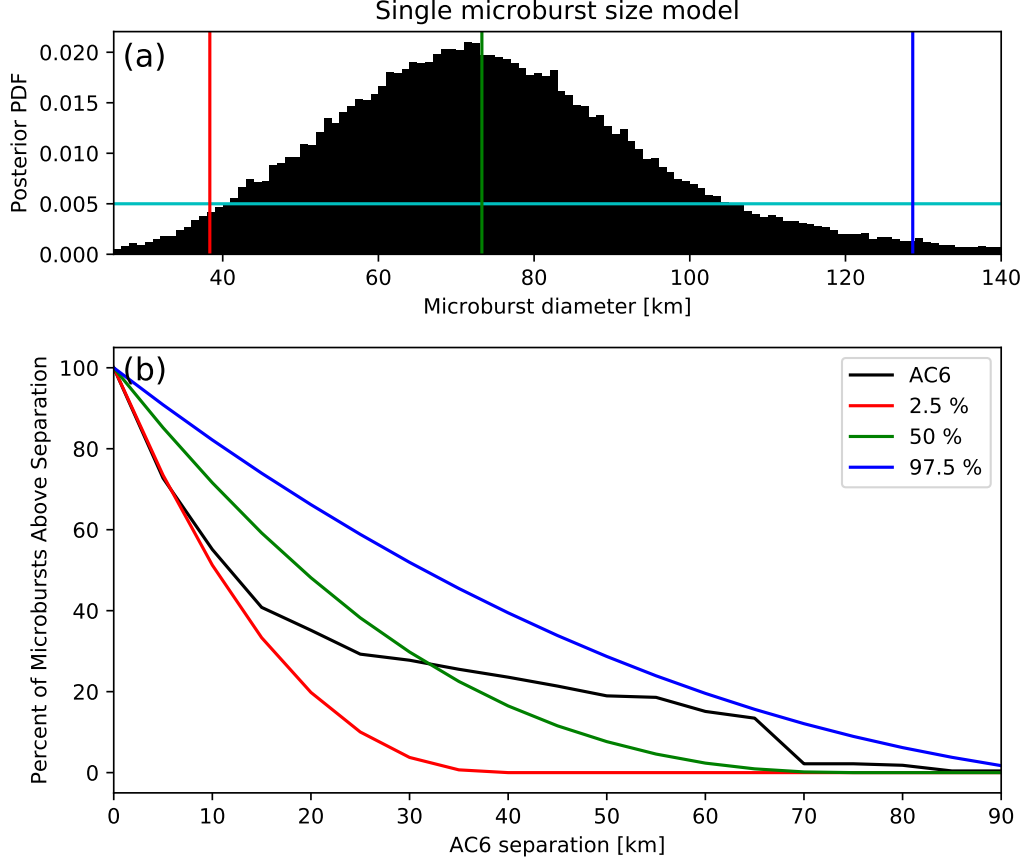


Figure 6. Range of plausible microburst sizes assuming all microbursts are one fixed size. Panel (a) shows the posterior probability density function of microburst diameters in black. The red, green, and blue vertical lines at 38, 73, and 129 km represent the 2.5, 50, and 97.5 posterior percentiles, respectively. A uniform prior between 0 and 200 km was assumed for this MCMC run and is shown in cyan. Panel (b) shows the percent of microbursts observed above an AC6 separation for $4 < L < 8$ in black. The 2.5, 50 and 97.5 size percentiles were estimated from the posterior and plotted in red, green, and blue curves, respectively.

of microbursts, have a diameter between 12 and 47 km with a rare population with a diameter between 76 and 234 km. The set of parameters that minimize least squares is 99.5 % of microbursts are small with a size of 21 km and the remaining 0.5 % of microbursts have a 140 km size.

Other, continuous PDFs were tested including: Maxwellian (Maxwell – Boltzmann), log-normal, and Weibull. The range of model parameters that are consistent with the observed $\bar{F}(s)$ are presented in Appendix Appendix B. These distributions were chosen because they have the following properties that are most realistic: they are continuous, approach 0 in the limit as $r \rightarrow 0$ (lower bound microburst size is ultimately limited by the electron gyroradius), and can be symmetrical or asymmetrical.

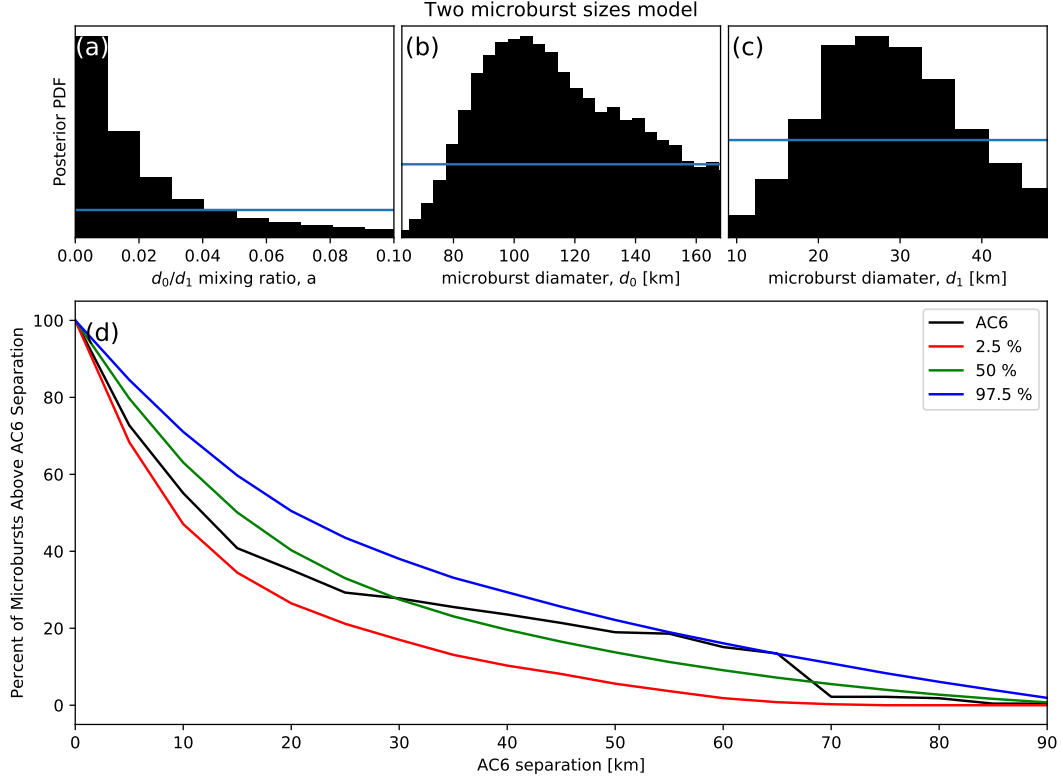


Figure 7. Plausible microburst percent curves assuming microburst size distribution is bi-modal consisting of two sizes d_0 and d_1 with a mixing term that quantifies the relative occurrence of the d_0 to d_1 microburst populations. Panel (a) shows the posterior distribution for the microburst population mixing term, a with a median value of 0.02. The a prior was uniform between 0 and 0.2. Panel (b) shows the posterior distribution for d_0 , the larger microburst population estimated with a uniform prior between 50 and 200 km and the posterior median diameter of 122 km. Panel (c) shows the posterior distribution for d_1 , the smaller microburst population, estimated using a uniform prior between 0 and 50 km with a median diameter of 28 km. Panel (d) is similar to Fig. 6b and shows the AC6 microburst fraction for $4 < L < 8$ in black. A set of 1000 random parameter triples (a , d_0 , and d_1) were drawn from the posterior and used to generate a family of $\bar{F}(s)$ curves. At each s the range of consistent $\bar{F}(s)$ were quantified by the 2.5, 50 and 97.5 percentiles and shown with the red, green, and blue curves, respectively.

6 Discussion

The LEO microburst $\bar{F}(s)$ estimated in section 4.2 shows that a majority of co-incident microbursts were observed by AC6 when they were separated by less than a few tens of km. This conclusion is consistent with prior literature and most similar to Parks (1967) who reported that many > 15 keV microbursts are less than 40 km in diameter while others were on average 80 ± 28 km in diameter. Furthermore, these results are similar to the bouncing packet example shown in J. Blake et al. (1996) with a size of “at least a few tens of kilometers”. The relatively small number of large > 70 km microbursts observed by AC6 fit in well with the results from Barcus et al. (1966) and Brown et al. (1965), although the AC6 separation is mostly latitudinal while Barcus et al. (1966) and Brown et al. (1965) used data from pairs of balloons separated predominantly in longitude.

Without knowledge of the microburst shape, a direct comparison between the AC6 and balloon observations is difficult. Trefall et al. (1966) discussed how a hypothetical circular microburst at the scattering location near the magnetic equator will be stretched into an ellipse with a semi-major axis in the longitudinal direction. This stretching effect should be explored further as it introduces an ambiguity from the eccentricity of the ellipse that prevents a direct latitudinal and longitudinal comparison.

When comparing our results to more recent studies, the AC6 microburst size distribution is much larger than the sizes reported in Dietrich et al. (2010) who used very low (VLF) frequency transmission paths and SAMPEX to conclude that microbursts must be smaller than 4 km from a small number of microbursts observed during one SAMPEX radiation belt pass. Dietrich et al. (2010) arrived at their conclusion by looking for temporal coincidence of microbursts and FAST events, subsecond VLF transmission perturbations, but the connection between FAST events and microbursts is not well understood. Lastly, our results are consistent with FIREBIRD-II observations of a > 11 km microburst reported by Crew et al. (2016), and the minority of microbursts observed by AC6 up to $s \approx 70$ km are consistent with the > 51 km bouncing packet microburst reported in Shumko et al. (2018).

The microburst PDF shown in Fig. 3b suggests that the microburst size distribution is bimodal. This has been suggested before by J. Blake et al. (1996) who noted that the > 150 keV and > 1 MeV microbursts are not always well correlated e.g. Fig. 10 in J. Blake et al. (1996). The quality of the AC6 data is insufficient to definitively conclude that there are two distinct microburst populations. The different microburst population hypothesis can be better tested with an AC6-like mission with better energy resolution and homogeneous MLT coverage.

The model results from section 5 emphasize that care must be taken when comparing the $\bar{F}(s)$ curves observed by AC6 and the true microburst size distribution due to the compounding effect of an unknown microburst size distribution, unknown microburst shape, and random microburst locations near AC6. By assuming there is only one microburst size, the results in Fig. 6 suggest that there is a 95% probability that the microburst diameter is somewhere between 38 and 129 km, a relatively wide range of values. On the other hand, the two-size model has a smaller variance around the AC6 $\bar{F}(s)$, which is expected with the addition of two more free parameters. The two size model is interpreted as 98% of microbursts diameters are between 12 and 47 km and larger microbursts are very uncommon.

A variety of continuous $p(d)$ such as the Maxwellian, Weibull and log-normal were also tested. While the continuous microburst PDFs are more realistic, there is no clear choice of which microburst PDF nature prefers. The one and two-size model are simple to interpret, and the two-size model qualitatively fits the observations the best out of all $p(d)$ tested. Surely nature does not only have two discrete microburst sizes. Rather,

the current evidence and reasoning supports a bimodal and continuous PDF hypothesis. Due to lack of prior observations and theoretical predictions, it is difficult to identify and test a more appropriate $p(d)$ hypothesis at this time.

The equatorial microburst $\bar{F}(s)$ estimated in section 4.2 and Fig. 4b in particular shows that the majority of microbursts were observed when the equatorial AC6 separation was less than 200 km. We will now explore how these results compare to prior multi-point measurements of chorus source sizes made near the magnetic equator. The International Sun-Earth Explorers (ISEE 1 and 2) were used by Gurnett et al. (1979) to make one of the first direct chorus source scale measurements. Gurnett et al. (1979) estimated that the wave power correlation scale was on the order of a few hundred km across the background magnetic field. Using the Cluster Wide Band Data measurements Santolik et al. (2003) found the correlation scale of whistler mode chorus waves to be around 100 km near the source region at $L \approx 4$ and midnight MLT sector. Furthermore, Turner et al. (2017) used the four satellites comprising the Magnetospheric Multiscale Mission and found that rising tone whistler mode chorus elements were phase coherent up to 70 km at $L \approx 8$. Agapitov et al. (2010, 2011, 2017, 2018) used multiple sets of spacecraft missions with wave measurements near the chorus source region to statistically show that the extent of chorus source region can extend from 600 km in the outer radiation belt to greater than 1,000 km in the outer magnetosphere. Most recent chorus study was published by Shen et al. (2019) who used mostly dual RBSP spacecraft wave measurements and found that the characteristic coherence size of lower band chorus waves transverse to the background magnetic field was $\approx 315 \pm 32$ km in the five to six L shell range. Shen et al. (2019) also found that the lower band chorus waves were slightly asymmetric and larger in the azimuthal direction. If this asymmetry is significant, then the eccentricity of the hypothesized elliptical microburst footprint is further increased in the longitudinal direction. **Add a few sentences regarding the wave-chorus distribution plots in Appendix C.**

The equatorial microburst size of less than a few hundred km shows that the waves responsible for scattering microburst electrons must have correlated properties on those scales. The wave properties necessary for scattering microburst electrons e.g. coherence, polarization, wave normal angle, etc. can be identified by studying the waves properties that are only observed by multiple equatorial spacecraft at small separations. These properties can then aid wave-particle scattering model development by constraining the wave properties and scattering modes responsible for scattering microburst electrons. In turn, future models could then make predictions regarding the distribution of microburst sizes in LEO.

7 Conclusions

In conclusion, the twin AC6 CubeSats enabled the detailed statistical study of microburst sizes from a two point measurement platform. Roughly 60% of the > 35 keV microbursts were simultaneously observed while AC6 was separated by less than 20 km and the rest were observed up to ≈ 70 km separation. Modeling the microburst cumulative distribution function is essential to quantify the relationship between the number of microbursts observed as a function of separation to a hypothesized microburst size distributions. The AC6 microburst data, together with modeling, has hinted at the existence of a bimodal microburst size PDF with the majority of microbursts with a diameter smaller than 40 km and a rare microburst population with a diameter around 100 km. The bimodal size hypothesis may be more comprehensively addressed from LEO spacecraft with more simultaneous microburst observations, homogeneous MLT coverage, and differential energy channels. Moreover, to disentangle the compounding effect that affects two-point microburst measurements, a X-ray imager on a high altitude balloon can observe the atmospheric microburst footprint and determine the microburst size, shape, and any spatial correlations with little ambiguity.

When mapped to the magnetic equator, most microbursts were observed while the mapped AC6 separation was less than 200 km. This correlates well with the sizes of highly correlated chorus waves and it suggests that the wave properties crucial for scattering microbursts must be correlated over relatively small regions. By studying the wave properties that are correlated on a few hundred km scales, the dominant wave scattering modes may be identified.

Appendix A Analytic Derivation of $\bar{F}(s)$

Here we derive the integral form of $\bar{F}(s)$ under the following assumptions:

1. microbursts are circular with radius r
2. microbursts are randomly and uniformly distributed around AC6

and the area $A(r, s)$, given in Eq. 4 and copied here for convenience

$$A(r, s) = 2r^2 \cos^{-1} \left(\frac{s}{2r} \right) - \frac{s}{2} \sqrt{4r^2 - s^2}. \quad (\text{A1})$$

A circular microburst whose center lies in $A(r, s)$ will be observed by both AC6 units and is counted in $\bar{F}(s)$. Now we derive the integral form of $\bar{F}(s)$ that accounts for the different spacecraft separations and microburst sizes that are distributed by a hypothesized PDF $p(r, \theta)$.

First we will account for the effects of various spacecraft separation, assuming all microbursts are one size. For reference choose of radius, r_0 and spacecraft separation, s_0 such that $A(r_0, s_0) > 0$ which implies that some number of microbursts, n_0 will be simultaneously observed. Now, if for example the spacecraft separation (or microburst radius) is changed such that the area doubles, the second assumption implies that the number of microbursts observed during the same time interval must double as well. This can be expressed as

$$\frac{n_0}{A(r_0, s_0)} = \frac{n}{A(r, s)} \quad (\text{A2})$$

and interpreted as the conservation of the microburst area density. By rewriting Eq. A2 as

$$n(r, s) = \left(\frac{n_0}{A(r_0, s_0)} \right) A(r, s) \quad (\text{A3})$$

it is more clear that the number of microbursts of size r observed at separation s is just $A(r, s)$ scaled by the reference microburst area density. The cumulative number of microbursts observed above s is then

$$N(r, s) = \int_s^\infty n(r, s') ds' = \left(\frac{n_0}{A(r_0, s_0)} \right) \int_s^\infty A(r, s') ds'. \quad (\text{A4})$$

Lastly, $\bar{F}(s)$ for a single r is then

$$\bar{F}(s) = \frac{N(s)}{N(0)} = \frac{\int_s^\infty A(r, s') ds'}{\int_0^\infty A(r, s') ds'} \quad (\text{A5})$$

To incorporate a continuous microburst PDF such as $p(r) = p_1 \delta(r - r_1) + p_2 \delta(r - r_2) + \dots$ we sum up the weighted number of microbursts that each size contributes to $N(s)$ i.e.

$$N(s) = \left(\frac{n_0}{A(r_0, s_0)} \right) \left(\int_s^\infty p_1 A(r_1, s') ds' + \int_s^\infty p_2 A(r_2, s') ds' + \dots \right) \quad (\text{A6})$$

The last step is to convert the sum of Dirac Delta functions into a continuous PDF $p(r)$ after which

$$N(s) = \left(\frac{n_0}{A(r_0, s_0)} \right) \int_s^\infty \int_0^\infty A(r, s') p(r) dr ds'. \quad (\text{A7})$$

With these considerations, $\bar{F}(s)$ is then given by

$$\bar{F}(s, \theta) = \frac{\int_s^\infty \int_0^\infty A(r, s') p(r, \theta) dr ds'}{\int_0^\infty \int_0^\infty A(r, s') p(r, \theta) dr ds'} \quad (\text{A8})$$

Appendix B Most probable parameter values for continuous microburst PDFs

Besides the one and two-size microburst models described in the main text, continuous PDFs such as the log-normal, Weibull, and Maxwellian were fit and their optimal parameters presented here.

For the Maxwellian PDF, we assumed the following form

$$p(r|a) = \sqrt{\frac{2}{\pi}} \frac{r^2 e^{-r^2/(2a^2)}}{a^3}. \quad (\text{B1})$$

The range of a consistent with the observed data was found to be between 0 and 35 km. Next, the log-normal distribution of the following form was used

$$p(r|\mu, \sigma) = \frac{1}{\sigma r \sqrt{2\pi}} e^{\left(-(\ln(r) - \ln(\mu))^2 / (2\sigma^2) \right)} \quad (\text{B2})$$

and the results are summarized in B1. Lastly the Weibull distribution of the following form was tested

$$p(r|c, r_0, \lambda) = c \left(\frac{r - r_0}{\lambda} \right)^{c-1} \exp \left(- \left(\frac{r - r_0}{\lambda} \right)^c \right). \quad (\text{B3})$$

for which the model parameters are summarized in Table B2.

Table B1. Range of log-normal model parameters consistent with the observed AC6 $\bar{F}(s)$

percentile (%)	μ	σ
2.5	1.8	0
50	21.8	0.4
97.5	52.0	1.1

Table B2. Range of Weibull model parameters consistent with the observed AC6 $\bar{F}(s)$

percentile (%)	c	r_0	λ
2.5	0.6	1.3	2.7
50	5.5	26.2	32
97.5	19.3	72.5	72.2

Appendix C Comparison of microburst to whistler mode chorus $\bar{F}(s)$

In this appendix we compare the equatorial distribution of microbursts sizes to the distribution of lower band whistler mode chorus waves near the magnetic equator. The wave data was obtained with the Time History of Events and Macroscale Interactions during Substorms (THEMIS) spacecraft over a 10 year period. Here we provide a brief overview of the procedure used identify chorus waves which is described in more detail in Agapitov et al. (2018). The THEMIS search coil magnetometer instrument was used to make magnetic field measurements in six logarithmically-spaced frequency channels between 1-4 kHz. This data was then used to cross-correlate the wave amplitudes between pairs of THEMIS spacecraft, to create a dataset of chorus waves simultaneously observed by THEMIS.

The spatial distribution of waves was found by first discarding wave detections with a cross-correlation less than 0.8. Then the wave dataset was split up into a low and high wave amplitude subsets with a 10 pT threshold. For each 75 km (rerun with 100 km) THEMIS separation bin, the probability of observing a coincident wave between a pair of THEMIS spacecraft was estimated. This probability is defined as the number of coincident low (high) amplitude waves observed, divided by the total number of low (high) amplitude waves observed. The result of this analysis is shown in Fig. C1.

The AC6 equatorial microburst dataset was analyzed in the same way to make a direct comparison. The probability of observing a coincident microburst for each equatorial separation bin (the cumulative estimates were not used) is shown in Fig. C2. The equatorial AC6 microburst probability has a similar shape to Fig. 4. Compared to the way that the coincident microburst dataset was analyzed and verified with $\bar{F}(s)$ in the main text, this approach has an unknown contribution from false positive detections in the denominator. Assuming the rate of false detections is not dependent on separation, this should have the effect of reducing the coincident probability evenly across all separations. This approach was not used in the main text because it is infeasible to clean the 8×10^4 total events in the dataset.

Include a brief discussion from the plots.

Acknowledgments

This work was made possible with the help from the many engineers and scientists at The Aerospace Corporation who designed, built, and operated AC6. M. Shumko was supported by NASA Headquarters under the NASA Earth and Space Science Fellowship Program - Grant 80NSSC18K1204. D.L. Turner is thankful for support from the Van Allen Probes mission and a NASA grant (Prime award number: 80NSSC19K0280). Other Aerospace and MSU funding sources... The AC6 data is available at <http://rbspgateway.jhuapl.edu/ac6> and the IRBEM-Lib version used for this analysis can be downloaded from <https://sourceforge.net/p/irbem/code/>

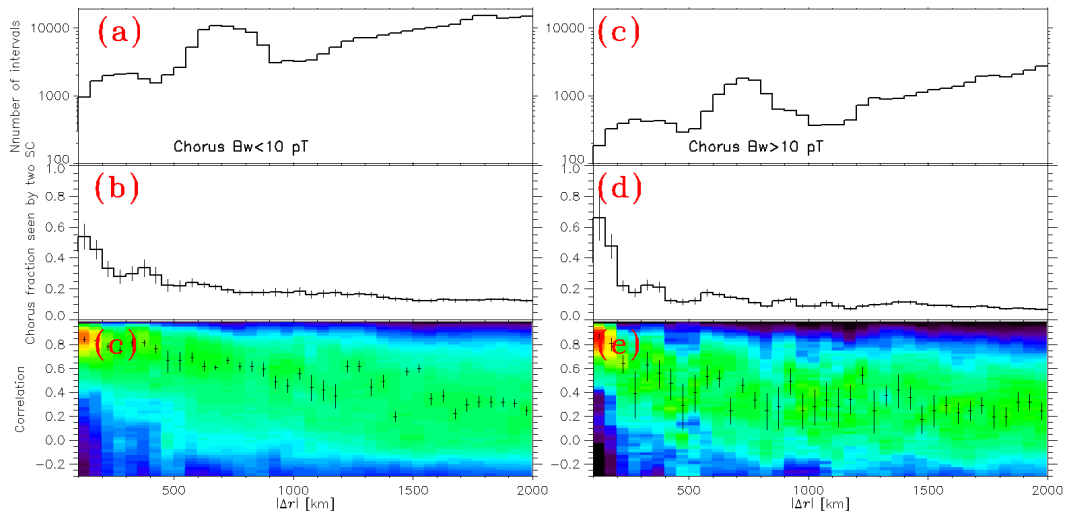


Figure C1. Placeholder for Oleksiy's plot from his 2018 paper.

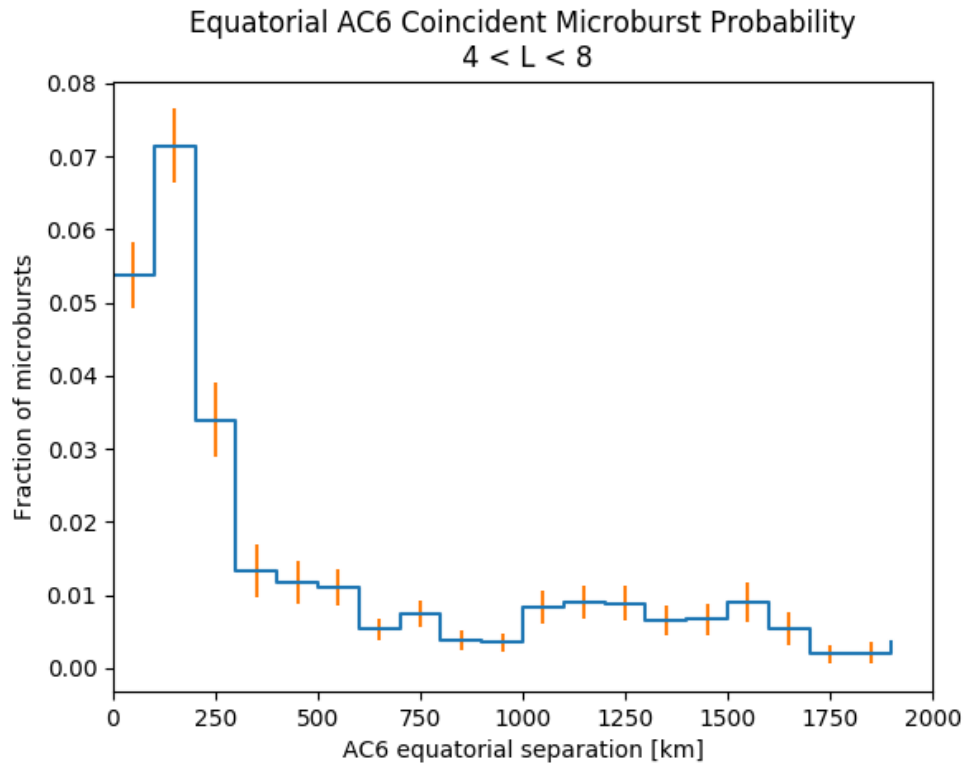


Figure C2. Placeholder. Plan to merge these two figures into one once I have access to Oleksiy's list of wave events.

References

- Abel, B., & Thorne, R. M. (1998). Electron scattering loss in earth's inner magnetosphere: 1. dominant physical processes. *Journal of Geophysical Research: Space Physics*, 103(A2), 2385–2396.
- Agapitov, O., Blum, L. W., Mozer, F. S., Bonnell, J. W., & Wygant, J. (2017). Chorus whistler wave source scales as determined from multipoint van allen probe measurements. *Geophysical Research Letters*, n/a–n/a. Retrieved from <http://dx.doi.org/10.1002/2017GL072701> (2017GL072701) doi: 10.1002/2017GL072701
- Agapitov, O., Krasnoselskikh, V., Dudok de Wit, T., Khotyaintsev, Y., Pickett, J. S., Santolik, O., & Rolland, G. (2011). Multispacecraft observations of chorus emissions as a tool for the plasma density fluctuations' remote sensing. *Journal of Geophysical Research: Space Physics*, 116(A9), n/a–n/a. Retrieved from <http://dx.doi.org/10.1029/2011JA016540> (A09222) doi: 10.1029/2011JA016540
- Agapitov, O., Krasnoselskikh, V., Zaliznyak, Y., Angelopoulos, V., Le Contel, O., & Rolland, G. (2010). Chorus source region localization in the earth's outer magnetosphere using themis measurements. *Annales Geophysicae*, 28(6), 1377–1386. Retrieved from <http://www.ann-geophys.net/28/1377/2010/> doi: 10.5194/angeo-28-1377-2010
- Agapitov, O., Mourenas, D., Artemyev, A., Mozer, F., Bonnell, J., Angelopoulos, V., ... Krasnoselskikh, V. (2018). Spatial extent and temporal correlation of chorus and hiss: Statistical results from multipoint themis observations. *Journal of Geophysical Research: Space Physics*, 123(10), 8317–8330.
- Anderson, K. A., & Milton, D. W. (1964). Balloon observations of X rays in the auroral zone: 3. High time resolution studies. *Journal of Geophysical Research*, 69(21), 4457–4479. Retrieved from <http://dx.doi.org/10.1029/JZ069i021p04457> doi: 10.1029/JZ069i021p04457
- Barcus, J., Brown, R., & Rosenberg, T. (1966). Spatial and temporal character of fast variations in auroral-zone x rays. *Journal of Geophysical Research*, 71(1), 125–141.
- Blake, J., Looper, M., Baker, D., Nakamura, R., Klecker, B., & Hovestadt, D. (1996). New high temporal and spatial resolution measurements by sampex of the precipitation of relativistic electrons. *Advances in Space Research*, 18(8), 171 - 186. Retrieved from <http://www.sciencedirect.com/science/article/pii/0273117795009698> doi: [http://dx.doi.org/10.1016/0273-1177\(95\)00969-8](http://dx.doi.org/10.1016/0273-1177(95)00969-8)
- Blake, J. B., & O'Brien, T. P. (2016). Observations of small-scale latitudinal structure in energetic electron precipitation. *Journal of Geophysical Research: Space Physics*, 121(4), 3031–3035. Retrieved from <http://dx.doi.org/10.1002/2015JA021815> (2015JA021815) doi: 10.1002/2015JA021815
- Blum, L., Li, X., & Denton, M. (2015). Rapid MeV electron precipitation as observed by SAMPEX/HILT during high-speed stream-driven storms. *Journal of Geophysical Research: Space Physics*, 120(5), 3783–3794. Retrieved from <http://dx.doi.org/10.1002/2014JA020633> (2014JA020633) doi: 10.1002/2014JA020633
- Bortnik, J., Thorne, R., & Inan, U. S. (2008). Nonlinear interaction of energetic electrons with large amplitude chorus. *Geophysical Research Letters*, 35(21).
- Boscher, D., Bourdarie, S., O'Brien, P., Guild, T., & Shumko, M. (2012). *Irbem-lib library*.
- Breneman, A., Crew, A., Sample, J., Klumpar, D., Johnson, A., Agapitov, O., ... others (2017). Observations directly linking relativistic electron microbursts to whistler mode chorus: Van allen probes and FIREBIRD II. *Geophysical Research Letters*.
- Brown, R., Barcus, J., & Parsons, N. (1965, 6). Balloon observations of auroral zone

- x rays in conjugate regions. 2. microbursts and pulsations. *Journal of Geophysical Research (U.S.)*, 70. doi: 10.1029/JZ070i011p02599
- Crew, A. B., Spence, H. E., Blake, J. B., Klumpar, D. M., Larsen, B. A., O'Brien, T. P., ... Widholm, M. (2016). First multipoint in situ observations of electron microbursts: Initial results from the NSF FIREBIRD II mission. *Journal of Geophysical Research: Space Physics*, 121(6), 5272–5283. Retrieved from <http://dx.doi.org/10.1002/2016JA022485> (2016JA022485) doi: 10.1002/2016JA022485
- Dietrich, S., Rodger, C. J., Clilverd, M. A., Bortnik, J., & Raita, T. (2010). Relativistic microburst storm characteristics: Combined satellite and ground-based observations. *Journal of Geophysical Research: Space Physics*, 115(A12).
- Douma, E., Rodger, C. J., Blum, L. W., & Clilverd, M. A. (2017). Occurrence characteristics of relativistic electron microbursts from SAMPEX observations. *Journal of Geophysical Research: Space Physics*, 122(8), 8096–8107. Retrieved from <http://dx.doi.org/10.1002/2017JA024067> (2017JA024067) doi: 10.1002/2017JA024067
- Greeley, A., Kanekal, S., Baker, D., Klecker, B., & Schiller, Q. (2019). Quantifying the contribution of microbursts to global electron loss in the radiation belts. *Journal of Geophysical Research: Space Physics*.
- Gurnett, D., Anderson, R., Scarf, F., Fredricks, R., & Smith, E. (1979). Initial results from the isee-1 and-2 plasma wave investigation. *Space Science Reviews*, 23(1), 103–122.
- Hastings, W. K. (1970). Monte carlo sampling methods using markov chains and their applications.
- Horne, R. B., & Thorne, R. M. (2003). Relativistic electron acceleration and precipitation during resonant interactions with whistler-mode chorus. *Geophysical Research Letters*, 30(10). Retrieved from <http://dx.doi.org/10.1029/2003GL016973> (1527) doi: 10.1029/2003GL016973
- Joy, S., Kivelson, M., Walker, R., Khurana, K., Russell, C., & Ogino, T. (2002). Probabilistic models of the jovian magnetopause and bow shock locations. *Journal of Geophysical Research: Space Physics*, 107(A10), SMP–17.
- Li, W., Thorne, R., Angelopoulos, V., Bonnell, J., McFadden, J., Carlson, C., ... Auster, H. (2009). Evaluation of whistler-mode chorus intensification on the nightside during an injection event observed on the THEMIS spacecraft. *Journal of Geophysical Research: Space Physics*, 114(A1).
- Li, W., Thorne, R. M., Angelopoulos, V., Bortnik, J., Cully, C. M., Ni, B., ... Magnes, W. (2009). Global distribution of whistler-mode chorus waves observed on the THEMIS spacecraft. *Geophysical Research Letters*, 36(9). Retrieved from <http://dx.doi.org/10.1029/2009GL037595> (L09104) doi: 10.1029/2009GL037595
- Lorentzen, K. R., Blake, J. B., Inan, U. S., & Bortnik, J. (2001). Observations of relativistic electron microbursts in association with VLF chorus. *Journal of Geophysical Research: Space Physics*, 106(A4), 6017–6027. Retrieved from <http://dx.doi.org/10.1029/2000JA003018> doi: 10.1029/2000JA003018
- Lorentzen, K. R., Looper, M. D., & Blake, J. B. (2001). Relativistic electron microbursts during the GEM storms. *Geophysical Research Letters*, 28(13), 2573–2576. Retrieved from <http://dx.doi.org/10.1029/2001GL012926> doi: 10.1029/2001GL012926
- Meredith, N., Horne, R., Summers, D., Thorne, R., Iles, R., Heynderickx, D., & Anderson, R. (2002). Evidence for acceleration of outer zone electrons to relativistic energies by whistler mode chorus. In *Annales geophysicae* (Vol. 20, pp. 967–979).
- Metropolis, N., Rosenbluth, A. W., Rosenbluth, M. N., Teller, A. H., & Teller, E. (1953). Equation of state calculations by fast computing machines. *The journal of chemical physics*, 21(6), 1087–1092.

- 663 Millan, R., & Thorne, R. (2007). Review of radiation belt relativistic electron
664 losses. *Journal of Atmospheric and Solar-Terrestrial Physics*, 69(3), 362 -
665 377. Retrieved from [//www.sciencedirect.com/science/article/pii/](http://www.sciencedirect.com/science/article/pii/S1364682606002768)
666 [S1364682606002768](http://www.sciencedirect.com/science/article/pii/S1364682606002768) doi: <http://dx.doi.org/10.1016/j.jastp.2006.06.019>
- 667 Mozer, F. S., Agapitov, O. V., Blake, J. B., & Vasko, I. Y. (2018). Simulta-
668 neous observations of lower band chorus emissions at the equator and mi-
669 croburst precipitating electrons in the ionosphere. *Geophysical Research Let-*
670 *ters*. Retrieved from <http://dx.doi.org/10.1002/2017GL076120> doi:
671 10.1002/2017GL076120
- 672 O'Brien, T. P., Blake, J. B., & W., G. J. (2016, May). *Aerocube-6 dosimeter data*
673 *readme* (Tech. Rep. No. TOR-2016-01155). The Aerospace Corporation.
- 674 O'Brien, T. P., Looper, M. D., & Blake, J. B. (2004). Quantification of relativis-
675 tic electron microburst losses during the GEM storms. *Geophysical Research*
676 *Letters*, 31(4). Retrieved from <http://dx.doi.org/10.1029/2003GL018621>
677 (L04802) doi: 10.1029/2003GL018621
- 678 O'Brien, T. P., Lorentzen, K. R., Mann, I. R., Meredith, N. P., Blake, J. B., Fen-
679 nell, J. F., ... Anderson, R. R. (2003). Energization of relativistic elec-
680 trons in the presence of ULF power and MeV microbursts: Evidence for dual
681 ULF and VLF acceleration. *Journal of Geophysical Research: Space Physics*,
682 108(A8). Retrieved from <http://dx.doi.org/10.1029/2002JA009784> doi:
683 10.1029/2002JA009784
- 684 Olson, W. P., & Pfizter, K. A. (1982). A dynamic model of the magnetospheric
685 magnetic and electric fields for July 29, 1977. *Journal of Geophysical Research:*
686 *Space Physics*, 87(A8), 5943-5948. Retrieved from [http://dx.doi.org/](http://dx.doi.org/10.1029/JA087iA08p05943)
687 [10.1029/JA087iA08p05943](http://dx.doi.org/10.1029/JA087iA08p05943) doi: 10.1029/JA087iA08p05943
- 688 Parks, G. K. (1967). Spatial characteristics of auroral-zone X-ray microbursts. *Jour-*
689 *nal of Geophysical Research*, 72(1), 215-226.
- 690 Sambridge, M., Gallagher, K., Jackson, A., & Rickwood, P. (2006). Trans-
691 dimensional inverse problems, model comparison and the evidence. *Geophysical*
692 *Journal International*, 167(2), 528-542.
- 693 Santolik, O., Gurnett, D., Pickett, J., Parrot, M., & Cornilleau-Wehrlin, N. (2003).
694 Spatio-temporal structure of storm-time chorus. *Journal of Geophysical Re-*
695 *search: Space Physics*, 108(A7).
- 696 Sharma, S. (2017). Markov chain monte carlo methods for bayesian data analysis in
697 astronomy. *Annual Review of Astronomy and Astrophysics*, 55, 213-259.
- 698 Shen, X.-C., Li, W., Ma, Q., Agapitov, O., & Nishimura, Y. (2019). Statistical
699 analysis of transverse size of lower band chorus waves using simultaneous mul-
700 tisatellite observations. *Geophysical Research Letters*, 46(11), 5725-5734.
- 701 Shumko, M., Sample, J., Johnson, A., Blake, B., Crew, A., Spence, H., ... Han-
702 dley, M. (2018). Microburst scale size derived from multiple bounces of
703 a microburst simultaneously observed with the firebird-ii cubesats. *Geo-*
704 *physical Research Letters*, 45(17), 8811-8818. Retrieved from [https://](https://agupubs.onlinelibrary.wiley.com/doi/abs/10.1029/2018GL078925)
705 agupubs.onlinelibrary.wiley.com/doi/abs/10.1029/2018GL078925 doi:
706 10.1029/2018GL078925
- 707 Thorne, R. M., O'Brien, T. P., Shprits, Y. Y., Summers, D., & Horne, R. B. (2005).
708 Timescale for MeV electron microburst loss during geomagnetic storms. *Jour-*
709 *nal of Geophysical Research: Space Physics*, 110(A9). Retrieved from [http://](http://dx.doi.org/10.1029/2004JA010882)
710 dx.doi.org/10.1029/2004JA010882 (A09202) doi: 10.1029/2004JA010882
- 711 Trefall, H., Bjordal, J., Ullaland, S., & Stadsnes, J. (1966). On the extension
712 of auroral-zone x-ray microbursts. *Journal of Atmospheric and Terrestrial*
713 *Physics*, 28(2), 225-233.
- 714 Tsurutani, B. T., Lakhina, G. S., & Verkhoglyadova, O. P. (2013). Energetic elec-
715 tron (> 10 keV) microburst precipitation, ~ 5 -15 s x-ray pulsations, chorus, and
716 wave-particle interactions: A review. *Journal of Geophysical Research: Space*
717 *Physics*, 118(5), 2296-2312.

- 718 Turner, D., Lee, J., Claudepierre, S., Fennell, J., Blake, J., Jaynes, A., ... others
 719 (2017). Examining coherency scales, substructure, and propagation of whistler
 720 mode chorus elements with magnetospheric multiscale (mms). *Journal of*
 721 *Geophysical Research: Space Physics*, 122(11).
 722 Van Allen, J. A. (1959). The geomagnetically trapped corpuscular radiation. *Journal*
 723 *of Geophysical Research*, 64(11), 1683–1689. Retrieved from [http://dx.doi](http://dx.doi.org/10.1029/JZ064i011p01683)
 724 [.org/10.1029/JZ064i011p01683](http://dx.doi.org/10.1029/JZ064i011p01683) doi: 10.1029/JZ064i011p01683
 725 Vernov, S., & Chudakov, A. (1960). Investigation of radiation in outer space. In *In-*
 726 *ternational cosmic ray conference* (Vol. 3, p. 19).
 727 Woodger, L., Halford, A., Millan, R., McCarthy, M., Smith, D., Bowers, G., ...
 728 Liang, X. (2015). A summary of the BARREL campaigns: Technique for
 729 studying electron precipitation. *Journal of Geophysical Research: Space*
 730 *Physics*, 120(6), 4922–4935.